Development 140, 4426-4434 (2013) doi:10.1242/dev.096768

Pulse propagation by a capacitive mechanism drives embryonic blood flow

Halina Anton[1,*], Sebastien Harlepp[2], Caroline Ramspacher[1], Dave Wu[1], Fabien Monduc[1], Sandeep Bhat[3], Michael Liebling[3], Camille Paoletti[1], Gilles Charvin[1], Jonathan B. Freund[4] and Julien Vermot[1,‡]

SUMMARY

Pulsatile flow is a universal feature of the blood circulatory system in vertebrates and can lead to diseases when abnormal. In the embryo, blood flow forces stimulate vessel remodeling and stem cell proliferation. At these early stages, when vessels lack muscle cells, the heart is valveless and the Reynolds number (Re) is low, few details are available regarding the mechanisms controlling pulses propagation in the developing vascular network. Making use of the recent advances in optical-tweezing flow probing approaches, fast imaging and elastic-network viscous flow modeling, we investigated the blood-flow mechanics in the zebrafish main artery and show how it modifies the heart pumping input to the network. The movement of blood cells in the embryonic artery suggests that elasticity of the network is an essential factor mediating the flow. Based on these observations, we propose a model for embryonic blood flow where arteries act like a capacitor in a way that reduces heart effort. These results demonstrate that biomechanics is key in controlling early flow propagation and argue that intravascular elasticity has a role in determining embryonic vascular function.

KEY WORDS: Biomechanics, Blood vessels, Hemodynamics, Low Reynolds number, Zebrafish

INTRODUCTION

Embryonic blood flow is essential for proper organogenesis and angiogenesis. Whether it is through the transport of oxygen and nutrients or via exertion of physical forces, blood flow has been shown to be instrumental in controlling gene expression and endothelial cell behavior in the embryo (Jones, 2011; Freund et al., 2012). Genome-wide expression analysis in cell culture shows that endothelial cells discriminate between multiple flow profiles by expressing different sets of genes (Boon and Horrevoets, 2009) and regulating basic cell functions (Hahn and Schwartz, 2008). Furthermore, flow forces have been shown to control heart development, patterning of the vascular network and hematopoiesis in vertebrates (Hove et al., 2003; le Noble et al., 2004; Yashiro et al., 2007; Adamo et al., 2009; North et al., 2009; Vermot et al., 2009; Buschmann et al., 2010; Liu et al., 2010; Nicoli et al., 2010; Bussmann et al., 2011; Corti et al., 2011; Chen et al., 2012; Lin et al., 2012). Nevertheless, despite the crucial role of blood flow in cardiovascular development (Jones, 2011; Freund et al., 2012), very little is known about flow forces propagation at the embryonic scales, where viscous forces dominate. Because of the intricacies of the physical properties of blood flow *in vivo*, particularly the three-dimensional arrangements of blood vessels and the sophisticated dynamics of the heart, it is necessary to address the mechanics of blood motion *in vivo*. Importantly, oscillations in pulsatile flow and subsequent wave reflections in blood vessels are the prominent physical features that control the mechanical stimuli involved in vascular flow and function in adult tissues (Zamir, 2000). Because the relative importance of viscosity can lead to flow characteristics that will dictate the forces experienced by endothelial cells *in vivo*, we probed the vascular hydrodynamics and biomechanics at work in the embryonic vascular system.

[1]Institut de Génétique Moleculaire et Cellulaire, CNRS/INSERM/UdS, 1 rue Laurent Fries, BP10142, 67404 Illkirch, France. [2]Institut de Physique et de Chimie des Matériaux de Strasbourg, Université de Strasbourg, UMR 7504, 23 rue du Loess, 67034 Strasbourg, France. [3]Department of Electrical and Computer Engineering, University of California, Santa Barbara, CA 93106, USA. [4]University of Illinois at Urbana-Champaign, Urbana, IL 61801, USA.

*Present address: Laboratoire de Biophotonique et Pharmacologie, UMR 7213 CNRS, UdS, Faculté de Pharmacie, Illkirch, France
‡Author for correspondence (julien@igbmc.fr)

Accepted 12 August 2013

MATERIALS AND METHODS

Zebrafish

Zebrafish lines used in the study are wild-type AB, *Tg(flk1:eGFP)* (Jin et al., 2005), *Tg(flt1^{enh}:RFP)* (Bussmann et al., 2010) and *Tg(E1b:gal4-VP16)s1101t*, *Tg(UAS:NpHR-mCherry)s1003t* (Arrenberg et al., 2010). The embryos were raised at 28°C in the dark and treated with 1-phenyl-2-thiourea (PTU) (Sigma Aldrich) at 10 hpf to inhibit pigment formation. For the imaging, they were anesthetized with 0.02% tricaine solution and were mounted on a glass-bottom Petri dish embedded in 0.8% low melting point agarose (Sigma Aldrich). *gata1* and *kdrl* morpholino (MO) injections were performed as described previously (Vermot et al., 2009; Habeck et al., 2002).

Imaging

Confocal imaging was performed on a Leica TCP SP5 direct microscope using a low-magnification, water-immersion objective (Leica, 25×, N.A.=0.95). By using the resonant scanner, and depending on the number of lines per frame, the acquisition frame-rate varied between 50 and 200 fps.

Bright-field imaging experiments were performed on a Leica DMIRBE inverted microscope using a Photron SA3 high speed CMOS camera (Photron, San Diego, CA, USA). For the blood cell-tracking experiments, the time-lapse sequences were acquired at 250-500 Hz frame rate, in transmission configuration using white light illumination and a water immersion objective (Leica, 63×, N.A.=1.2).

The optomanipulating experiments were performed by adding a second halogen lamp and filter cube for activating the NpHR-mCherry light gated pump. A manual shutter was placed in the illumination path in order to control the illumination period. A low-magnification water-immersion objective (Leica, 20×, N.A.=0.7) was used for both imaging and delivering the green light activating the NpHR ion pump. The acquisition times were 10-20 seconds at 60-200 fps. The embryos did not show any sign of phototoxicity during or post acquisition.

All microscopy setups used were equipped with a heating device that ensured the embryos were kept at 28°C during the imaging.

The velocity of red blood cells was determined by manual tracking and kymograph analysis using ImageJ (NIH) and Matlab (MathWorks) software.

Optical tweezers

Optical tweezers experiments were performed using a home-built microscope described previously (Drobczynski et al., 2009). Briefly, the optical setup contains a laser (Spectra Physics YAG 1064 nm), focused through a high numerical aperture oil immersion objective (Zeiss, ×100, 1.25 N.A.). The light scattered by the trapped cell is collected through a second objective (Olympus, X40, 0.6 N.A.) before being imaged on a four-segment photodiode. The sum (ΣI) and the difference (ΔI) of the intensities collected by each segment are sampled at 4 kHz and digitized with a 16-bits resolution, using a National Instruments card NI PCIe-6259. The subsequent signal treatment was performed using LabView 7.2 (National Instruments) under Windows XP. The laser power used to trap the blood cells varied from 2 to 3 W (laser head output), depending on the location of the blood cell. The beam energy was dissipated by the flow, trapping blood cells without inducing any other side effect on the fish.

To visualize the sample we use a second path for the white light. The white light is brought to the setup with an optical fiber and collimated with the objective lens O3 (Leica, ×10, 0.3 N.A.). We imaged the sample using a Basler A602f CMOS camera for image acquisition at high frame acquisition (200 Hz). The camera was synchronized with the acquisition done on the photodiode in order to follow all motions (fish, blood cells and vessels). The setup allows following the blood cell displacement within the trap either with the quadrant photodiode or the Basler camera. Movies and photodiode traces were both used for subsequent analysis.

Video analysis and ϕ measurements

We used ImageJ and Wavemetrics IgorPro to analyze the motions of red blood cells within the trap. Stacks were realigned so that X or *y*-axis are aligned along the DA, X being in the axis and Y orthogonal to the DA. This allowed us to limit the cross contributions of the displacements in case the blood flow had an angle with respect to these axes. Once this angle was fixed, an orthogonal view on the center of the cell was performed to get the time trace. The traces were saved as a text file and IgorPro was then used to perform the quantitative analysis. Using the calibration curve, we transformed the orthogonal views in time and position graphs, taking into account the rotation applied during the first steps of analysis. The spatial resolution is 120 nm in both directions after treatments

We adjusted the time traces with a sine function to extract the frequency and phase. From these adjustments, we obtained the phase shift between both signals.

We confirmed the Y motion was not due to deformability of the DA by comparing the amplitude of motion of the blood cell with endothelial cells. On average, blood cell motion amplitude in Y is 10 times bigger than endothelial amplitude in the area of ISV attraction.

The anatomy and position of the ISV was extracted by analyzing the tracks and diameter of the blood cells flowing into it.

Photodiode data analysis

The photodiode directly converts the displacement of the blood cell from the trap center into a different voltage. We took a 4-second time trace with an acquisition frequency of 4 kHz. We then extracted the power spectrum from that time trace. This power spectrum directly showed the heart beat frequency and also the cut-off frequency f_c. This cut off frequency is directly correlated to the trap stiffness k_{Trap} by the following equation: $k_{Trap}=2\pi\zeta f_c$, where ζ is the friction of the blood cell.

This trap stiffness was then used to convert the displacement extracted from the movies into forces.

The theoretical hydrodynamic force applied to the blood cell can be given in first approximation by the formula $F_{hyd}= 6\pi\eta Rv$, where η represents the fluid viscosity (≈2.10^{-3} Pa.s), R the radius exposed to the fluid flow (≈1 μm) and v the fluid velocity (≈2000 μm/sec). The viscosity, η, was obtained using the method described below. This measure is overestimated due to the presence of the arterial walls. The calculated error is less than 15% and does not affect the general described behavior.

Given these values, the maximal hydrodynamic force exerted on the blood cell is around 75 pN. This value is taken in the center of the aorta and decreases when the blood cell approaches the membrane wall. The values found with the optical trap are thus in good agreement with the theoretical value calculated above.

Zebrafish mounting for tweezing experiments

The sample was mounted on a two-axes piezoelectric crystal (Physics Instruments GmbH, displacement range 0-100 μm, resolution 0.2 nm) perpendicular to the optical *z*-axis. Fish were incubated in a thermal bath regulated at 27°C until mounting on the sample holder consisting of a microscope slide with a hole, onto which a coverslip was fixed to both sides. The fish was adsorbed to one of the coverslips using 0.8% agarose in Danieau and then covered with 1% low melting point agarose (with 0.0001% lidocaine). Then, we placed this slide under the microscope for the observations. The room temperature was set to 24°C. The embryos were positioned in the microscopic framework in order to overlap the DA longitudinal axis with the *x*-axis and the ISV with the *y*-axis.

Plasma viscosity measurements

Viscosity was measured by particle tracking a cell nucleus in the dorsal aorta in a 2,3-butanedione monoxime (BDM)-treated fish injected with *gata1* MO. Fish were imaged at 20× magnification at 1000 Hz. Sub-pixel particle tracking was performed by fitting images of the nucleus to a two-dimensional Gaussian using custom Matlab software. We confirmed that the motion of the nucleus reflected the motion of the entire cell, and that the cell was not tethered to the vessel wall. The histogram of the motion was then fitted to the probability distribution function of a freely diffusing particle of equivalent size; the second moment then reflects diffusion coefficient:

$$\left\langle \Delta x^2 \right\rangle = 4D\Delta t \,.$$

As $D = k_BT(6\pi\eta a)^{-1}$ [where k_B is the Boltzmann constant, T (303 K) is the temperature and a (5 μm) is the radius of the tracked cell], the extracted viscosity is 0.0022±0.0007 Pa seconds.

Blood cell velocity measurements

Velocities were calculated by hand or by performing a kymograph along the direction of flow. The kymograph then shows space along one axis and time along the other axis, with time step Δt given by the frame-rate (between 250 and 500 fps). Cells that move along the direction of flow leave a trace in time as they move through the vessel in space. These traces were then segmented in Matlab using the Canny edge-finding algorithm. The segmented traces consisted of an image of pixels that trace out an approximate curve. The curves were then converted into coordinates by fitting a line through each nearest neighbor segment of the curve. The fit lines are median filtered through a 3-point filter to remove spurious noise. As many cells flow through the kymograph in a given Δt, the velocity in the vessel is constructed statistically by averaging the velocity of many cells at Δt of the kymograph. This procedure was performed for dorsal aorta, posterior cardinal vein and intersegmental vessels.

Circulation model and heart work calculation

The model is presented in the supplementary information. We used *Mathematica* to run our flow model (Wolfram Research). All the parameters used come from *in vivo* measurements. The model was validated against analytical solutions for small systems. All numerical results were confirmed to be independent of the resolution as set by the order of the polynomial basis functions. An adaptive time-stepping scheme assured time accuracy. In the analysis we neglected terms proportional to the radius change squared: δR^2. For changes in vessel radius of <10%, this is estimated to cause a 1% error and can therefore be considered small.

Heart work rate (Power) was calculated as follows. Heart work rate=Force × Velocity. We specified the inflow velocity based upon the data. The pressure was computed as part of solving the numerical model. The obtained pressure multiplied by the area of the aortic root gave the force.

RESULTS

Blood flow is rectified along the zebrafish embryonic vascular network

We performed high temporal resolution imaging in zebrafish to characterize the flow in the axial vascular network of the embryonic trunk (Fig. 1A,B). By 48 hours post-fertilization (hpf) blood circulates in most of the intersegmental vessels (ISVs) and by 72 hpf the network is fully functional (Ellertsdóttir et al., 2010). At these stages, the anatomy of the tubing network is relatively simple: blood cells move through one of the 15 or so loops closed by intersegmental artery-vein pairs between the dorsal aorta (DA) and the posterior cardinal vein (PCV) (Fig. 1B) (Weinstein and Fishman, 1996). We compared blood cell motion in the DA, the PCV and the intersegmental loops (Fig. 1C). In the DA, blood cell motion reflects the heartbeat rhythm with regular intermittent propagation of fluid and almost no flow in between the pulses (Fig. 1D). Interestingly, ISV flow is pulsatile but with a profile significantly different to that of the DA. Its peak flow is slower than in the DA (the velocity peak is 1200±300 μm/second compared with 2100±400 μm/second in the DA in the tail region at 48 hpf), and motion seldom ceases during an oscillatory cycle (Fig. 1D,E). By contrast, blood flow is relatively steady in the PCV (Fig. 1D). This corresponds to a 57% drop in the pulse amplitude, indicating a strong flow rectification between the two vessels. A particularly notable effect is observed near the ISV entry where cells were observed to move toward the heart in the opposite direction to the predominant DA flow (Fig. 1F-H). In some dramatic cases, blood flow in the ISV appears to be completely independent of DA flow (Fig. 1I-K; supplementary material Movie 1). Thus, the relationship between the flows of the ISV and DA is not simple and suggests that a strong flow rectification occurs between these two branches of the vascular network. This feature is key as it will affect perfusion and local hemodynamic stresses experienced by the vessels.

For pulsatile flow, it is important to recognize the pulse strength relative to viscous effects, which is quantified by the Womersley number [$Wm=R(\omega/\nu)^{1/2}$, where R is the vessel radius, ω the pulse frequency and ν the kinematic viscosity]. The low $Wm \approx 0.08$ of the zebrafish embryo at 72 hpf indicates that the cardiac frequency does

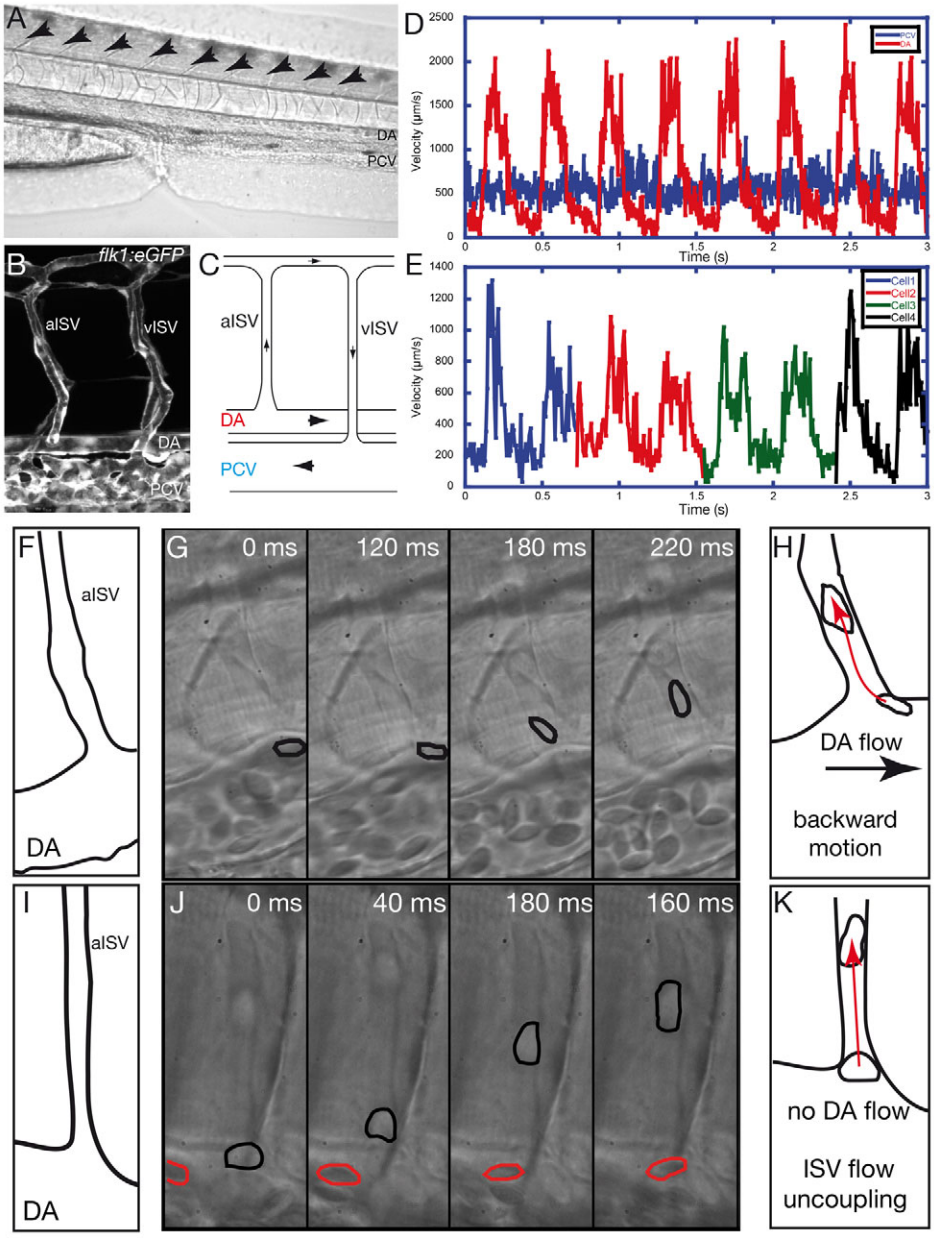

Fig. 1. Blood cell motions demonstrate flow rectification and an additional force at the ISV entry of the embryonic vascular network. (**A**) Lateral view of the zebrafish larvae at 72 hpf. Blood vessels of the tail are visible in the focal plane. Blood cells are present in the dorsal aorta (DA) and the posterior cardinal vein (PCV). Arrows indicate the intersegmental vessels (ISV). (**B**) View of a typical vascular loop between the DA and the PCV through *z* projection of a confocal stack obtained with the *Tg(flk1:eGFP)* transgenic line expressing the EGFP specifically in the endothelial cells. Arterial ISV (aISV) and venous ISV (vISV) are labeled. (**C**) A typical vascular loop observed in the trunk vasculature with the black arrows indicating the direction of blood flow. The blood cells in the DA enter into the aISV, pass in to vISV and move towards the PCV and the heart. (**D**) Typical velocity profile of the blood cells circulating in the DA (red) and PCV (blue). The DA displays a pulsatile flow, whereas the PCV flow is relatively steady. (**E**) Typical velocity pattern of blood cells observed in the ISV. Flow is pulsatile but not fully synchronized with the DA flow. (F-K) Fast imaging of blood cell motion at the ISV entry. (**F**) The observed topography at the ISV entry in G. (**G**) Fast time-lapse imaging showing a blood cell (outlined in black) moving against the DA flow towards the ISV. (**H**) Summary of the backward blood cell motion towards the ISV (red arrow) as opposed to DA flow (black arrow). (**I**) The observed topography at the ISV entry in J. (**J**) Fast time-lapse imaging showing blood cell displacement in the ISV (outlined in black) is much greater than in the DA (outlined in red). (**K**) Summary of the additional cell motion within the ISV (red arrow) when there is no visible DA flow.

not introduce significant inertia via the introduction of a fast time scale. In this context, the residual blood cell motion in the ISV in the absence of blood cell motion in the DA cannot be due to inertia, thus indicating an additional force generated in the network. At the same time, it is surprising in a low *Re* environment (where viscous forces dominate) that flow does not directly follow the pump in a closed network.

The dynamics of blood flow forces is complex at the ISV entry

To investigate the temporal and spatial relationships leading to the apparent attraction of blood cells towards the ISV entry, we developed a probing assay allowing the characterization of blood cell motion over time at a fixed location. Blood cells track the flow, but only at the locations of the cells, which move. It is thus nearly impossible to characterize blood cell motion at a point of the network over time using conventional cell tracking. To circumvent this limitation, we immobilized blood cells within an optical trap and followed their motion in response to flow as an indicator of flow direction. We trapped at 1064 nm, a non-phototoxic wavelength, so that embryonic and vascular development was not affected when compared with non-manipulated embryos from the same clutch (n=20). This approach allowed us to assess directly the *in vivo* pulsatile flow in the DA (Fig. 2A-C; supplementary material Movie 2) and to precisely investigate blood cell motion near the ISV entry. To suppress interference from other cells, we artificially decreased the number of circulating blood cells by inhibiting hematopoiesis through partial knockdown of *gata1*, a pro-hematopoietic transcription factor in zebrafish (Galloway et al., 2005). The obtained *Wm* in *gata1* morphants is 0.042 and is lower

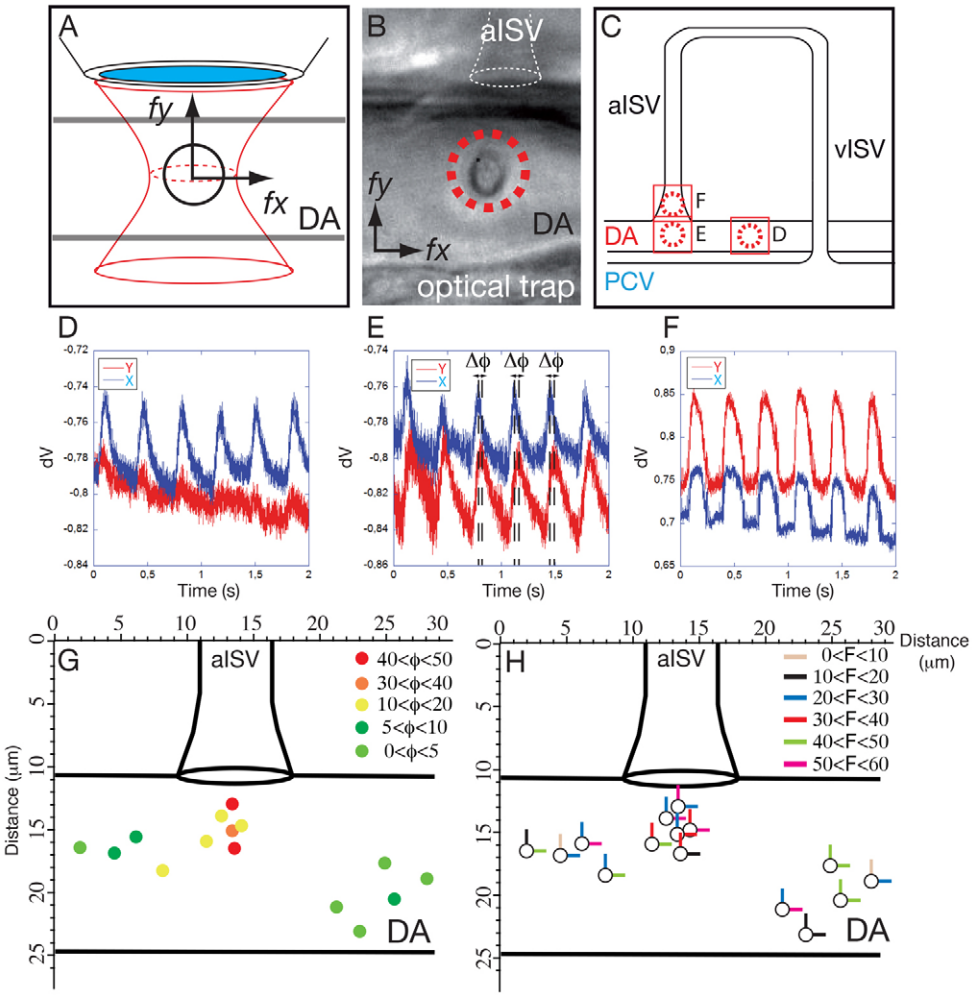

Fig. 2. Blood cell attraction towards the ISV follows two oscillatory phase-shifted forces. (**A**,**B**) Schematic representation (A) and *in vivo* live image (B) to detail the optical tweezing experiments undertaken to characterize blood cell motion near the ISV entry. Detection of the constrained blood cell motion within the optical tweezer reflects the effects of surrounding flow forces. The reconstruction of the displacement along the *x* and *y* axes allowed us to decipher the force applied to the cell (*fx* and *fy*). (**C**) *In vivo*, blood cells are trapped at different positions in the DA near and at the ISV entry, with dotted red circles representing the immobilizing focus of the optical tweezer in the same embryo (B,C). The corresponding motion patterns are shown in D-F. (**D-F**) Real-time blood cell displacement (represented by the signal from the quadrative detector, dV) is plotted as a function of time, illustrating the typical motion resulting from blood flow. When blood cells are positioned in the DA away from the ISV, the displacement along the *x*-axis is predominant, showing the effect of pulsatile flow in the DA (D). When positioned near the ISV entry, an additional motion in Y is observed that is always out of phase from the X direction (Δφ) (E). The attractive force is thus oscillating and is not fully coupled with DA flow. When positioned in the ISV, blood cell motion in X and Y directions are in phase again (F). (**G**) Phase-shift (Δφ) mapping at the ISV entry demonstrates the attractive force is correlated with the proximity to the ISV entry and shows the XY correlation decrease when closer to the ISV. (**H**) Force map in pN obtained after optical-tweezer measurement. The maps in G and H were obtained by analysing three different embryos.

than the controls due to the lower viscosity. Nevertheless, as the *Wm* is still near zero, the general flow features will be similar to the controls. Typically, trapped blood cells displayed an oscillatory movement (supplementary material Movie 2). The frequency associated with one cycle of blood cell motion was F=3.22±0.25 Hz, correlating with the frequency of the heartbeat and the motion profile of the non-trapped blood cells in the DA (3.21±0.88 Hz). Altogether, these data show that optical tweezers can be used to precisely probe flow in the vicinity of the ISV entrance.

In order to mark the transition between DA-dominated versus ISV-dominated flow, we investigated blood cell behavior at different distances from the ISV entrance. Typical time traces of the displacement of the trapped cells in different positions in the DA and ISV are shown in Fig. 2D-F. By comparing the time traces projected on the X and Y axes (Fig. 2C-F), we can define a phase shift ($\Delta\phi$) between the two motions. When trapped in the DA away from the ISVs (d >12 μm) (Fig. 2D), the displacement in X direction is dominant, which means that blood cells are advected along the DA and are entrained in the pulsatile, unidirectional flow. This leads to a highly correlated XY pattern ($\Delta\phi$=3.2±4.2°). By contrast, $\Delta\phi$ increases dramatically when blood cells are trapped near the ISV entry (Fig. 2E), showing that the attractive force in this area is out of phase with the DA flow ($\Delta\phi$=43±4° at 2.2 μm of the ISV entry). As shown in Fig. 2F, the X and Y movements are again synchronized in the ISV. These results indicate that a clear separation between a correlated and non-correlated XY movement can be seen close to the ISV entry, which is maximal when flow velocity is decreasing in the DA (Fig. 2D-G). To locate precisely the attractive area, we mapped $\Delta\phi$ at a higher spatial resolution in several embryos (n=4). Fig. 2G,H represent the obtained composite map of $\Delta\phi$ and measured forces, respectively. These maps confirm that near the ISV entry the $\Delta\phi$ is higher than in the DA. Using the optical tweezers as a picodynamometer, the displacements of the blood cells in the trap were converted into forces confirming that the orthogonal forces increase at the ISV entry (Fig. 2H). Altogether, these data confirm the presence of an attractive force and that the ISV influence can be detected several microns away from the ISV entry (6.5±2.5 μm) (Fig. 2G,H). Moreover, $\Delta\phi$ is maximal when the DA velocity is close to zero, indicating that flow is maintained near the ISV entry, after the heart-induced flow into the DA has ceased, at every cycle of contraction.

The embryonic dorsal aorta acts as a capacitor

To gain insight into the physical origins of the flow maintenance in the ISV, we developed a physical model of the vascular network that simulates the flow in a network representing the essential features of the zebrafish vascular anatomy. We hypothesized that vascular elasticity could provide a capacitance to the DA, which leads to the flow at the ISV entry and overall a rectification of the pulse. This mechanism is comparable in the current viscous limit to the so-called Windkessell effect occurring in the big arteries and vessels in the adult vascular network (Westerhof et al., 2009). We therefore developed a mathematical model of the zebrafish vascular network for Poiseuille flow in a distensible network (see supplementary material Appendix S1 for the complete description of the model).

We considered the vessels as straight, round tubes of radius R. They are distensible, with distensibility D defined as:

$$D \equiv \frac{1}{A}\frac{dA}{dp}, \qquad (1)$$

where $A=\pi R^2$ and p is the excess pressure in the tube above that of the local environment. We assume that the blood is a Newtonian fluid with viscosity μ. For the microvasculature, with tube diameters $2R$<100 μm and mean flow velocities $U\leqslant$1 mm/s, and assuming a blood kinematic viscosity $\nu=5\times10^{6}$m^2/s (about five times that of water), the Reynolds number is $Re=U(2R)/\nu\leqslant$0.02. Thus, inertia is anticipated to play at most a very small role. Similarly, for pulse rates <2/s the Womersley number is:

$$Wm \equiv R\left(\frac{\omega}{\nu}\right)^{\frac{1}{2}} \lesssim 0.04,$$

as observed *in vivo*.

In this low *Re*, low *Wm* limit, the Newtonian flow is Poiseuille, with the unidirectional streamwise velocity related to the streamwise pressure gradient as:

$$u(r) = -\frac{1}{4\mu}\frac{\partial p}{\partial x}\left(R^2 - r^2\right), \qquad (2)$$

where r is a radial coordinate in the tube measured from its axis. Integrating over the tube cross-section yields volumetric flow rate:

$$Q = \int_0^R u(r)2\pi r\,dr = -\frac{\pi R^4}{8\mu}\frac{\partial p}{\partial x}, \qquad (3)$$

which is a conserved quantity for a constant density fluid such as blood. The fourth-order dependence on the radius of this volume flux reflects a perhaps unintuitively strong dependence on vessel diameter that should be considered in interpreting results. The corresponding mean flow velocity is:

$$\bar{u} = \frac{Q}{A} = -\frac{R^2}{8\mu}\frac{\partial p}{\partial x}. \qquad (4)$$

Blood is well known to be modestly non-Newtonian in small vessels. A model with a more realistically blunted mean profile could be developed based upon the empirical data available. However, as these do not differ significantly from the Newtonian fluid model, for this study we consider a Poiseuille flow. Such a model is too crude to reproduce specific measurements exactly but usefully illustrates the key physical mechanisms (supplementary material Fig. S1). By fitting our *in vivo* measured parameters with the model, we could observe a rectified, less pulsatile, flow in the ISV, as seen in the embryo (Fig. 3A,B; supplementary material Movie 3). To confirm that the constant ISV flow was due to the elasticity of the network, we performed the same simulation without elasticity and found that ISV flow is fully correlated with the DA flow under this condition (Fig. 3C). Thus, features of ISV flow strongly depend on the DA elasticity. The DA is ‘inflated’ during the contraction phase of the heartbeat, and then more slowly ‘deflates’ via the ISV flow (Fig. 3B), thus literally acting as a capacitor. Importantly, the model suggests that flow rectification and the additional flow towards the ISV are part of the same biomechanical process.

We next investigated this biomechanical mechanism *in vivo*. The capacitor model presented above simply requires elasticity in elements of the network in order to build up an additional pressure gradient and induce a local net flow near the ISV. In zebrafish, many elements of the vascular network are elastic and could contribute to the capacitor effect. Nevertheless, the most prominent elastic deformation in the network is a drastic change in diameter of the DA during cycles of contraction (Fig. 3D-G; supplementary material Movie 4). Optical sections through 72 hpf *Tg(flk1:eGFP)* zebrafish DA, which expresses GFP in endothelial cells, were reconstructed into four-dimensional data sets (supplementary material Movie 5) to show the extent of the deformation along the

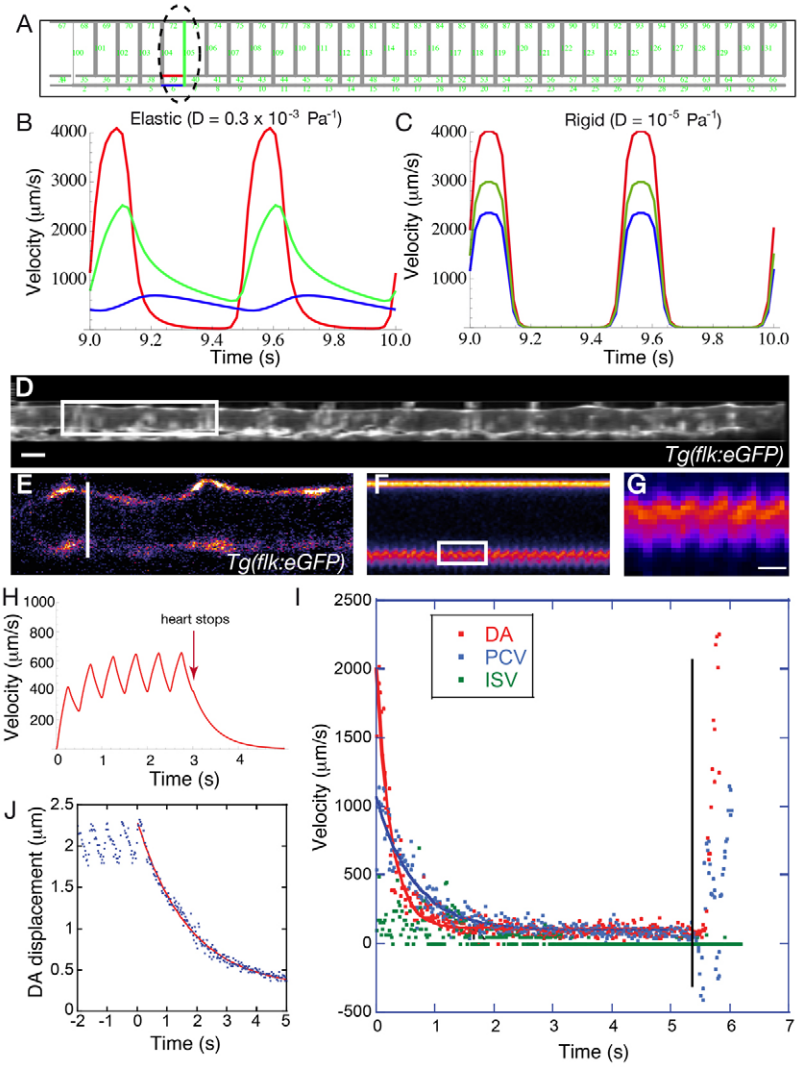

Fig. 3. The dorsal aorta conveys an elastic deformation that is coupled with a capacitive force. (**A**) The overall simulated network, designed to recapitulate the zebrafish vasculature. The numbers label the individual segments. (**B**) Flow patterns calculated at the sixth segment of the network elasticity (outlined with a dotted black line in A) show a strong flow rectification, as well as a delay between the flow velocity peaks when comparing DA and ISV flow. Arterial flow is in red, ISV flow in green and venous flow in blue. (**C**) Calculated flow profile without elasticity shows that the ISV flow directly tracks the DA. (**D**) Side view of the DA using *Tg(flk1:eGFP)* as a label of the endothelial cell walls reconstituted in 3D. Scale bar: 20 μm. (D-G) An elastic deformation is generated in the network at every heart contraction. (**E**) The distance between the dorsal and ventral wall of the DA (white bar) increases upon the heart contraction in synchrony with heartbeat. The box in D outlines the area shown in E. (**F**) Kymograph of the DA wall displacement over time recorded from the white bar in E. (**G**) Zoom of the kymograph boxed in F showing the regular deformation is visible over time and only on the ventral side of the DA. Scale bar: 420 ms. (**H**) Blood cell velocity plotted as a function of time after stopping the heartbeat predicted by the model. The blood cell motion in the DA does not stop immediately but the velocity decreased progressively over several seconds. (**I**) Blood cell velocity plotted as a function of time after stopping the heartbeat *in vivo* using *Tg(E1b:gal4-VP-16)s1011t*, *Tg(UAS:NpHR-mCherry)s1003t* at 5 dpf for optogenetics experiments. The time between the black lines corresponds to the duration the heart stopped beating after illumination at 488 nm. Motion is seen after heart stops as predicted by the model. (**J**) Movement of the DA ventral wall (DA displacement) following the stop in heart contraction [t=0 corresponds to light switch on (heart off)]. The experimental data were fitted to an exponential decay revealing the time constants of the decay after heart stops (t=0, when light switches on) showing a fast deflation of the DA when heart stops.

embryonic DA. We next assessed the possibility that the network builds up pressure driving a net flow within the smaller ISV vessels. Overall, such an effect predicts that flow should be possible even out of phase with the heart contraction for a period after the heart is stopped (Fig. 3H). To perform similar experiments *in vivo*, we used light activation of the halorhodopsin in the myocardium to stop the heart suddenly (Arrenberg et al., 2010) at 5 days post-fertilization (dpf), when heart valves are fully mature. As predicted, flow was visible for several seconds after heart contraction stopped (more than 5 seconds after heart stopped, Fig. 3I; supplementary material Movie 6) at 5 dpf. The displacement of the DA wall after the heart stop was measured and displayed a displacement with a similar profile over several seconds (Fig. 3J). As expected, the flow decay was also significant at 3 dpf (Fig. 4). These data indicate that the DA elasticity permits it to contain blood at pressure at each cycle of contraction and demonstrate that the DA acts as a capacitor.

ISVs set the resistivity of the network

A characteristic feature of tubular network, reflecting the R^4 dependence of flow rate on pressure drop in Eqn 3, is that the resistivity of the network is primarily mediated by the tubes of smaller diameter. In the embryonic vascular network, this would correspond to the ISV because they are much smaller than the DA and the PCV. Thus, we hypothesized the biomechanical origins of the flow decay comes from the ISV. To directly demonstrate the effect of decreasing the size of the ISV network on the flow decay, we knocked down *kdrl*, which is known to stop ISV network formation (Habeck et al., 2002). As expected, we found that *kdrl* knock down affects the vascular network structure, in particular ISV length, which is reduced (Fig. 4A,C). Overall, *kdrl* knock down led to a clear decrease in the combined ISV flow in the network at 3 dpf as less than 25% of the ISVs are functional (n=25) (Fig. 4B,D). As a consequence, *kdrl* knock down leads to an increased resistance in the network as a majority of ISVs are blocked. In the model, blocking 85% of the ISV leads to an increase in the relaxation timescale (Fig. 4E). *In vivo*, we found that the flow decay after heart stopping through optogenetics was significantly longer (33% increase, $t_{1/2}$=0.063±0.012 seconds in *kdrl* versus 0.042±0.005 seconds in wild type, n=6, P=0.05) (Fig. 4F). Together, these data demonstrate that the viscous resistance of the ISV flow sets the time scale of the flow decay in the controlled conditions of the model and in the *kdrl* morphants, where the ISV are blocked due to angiogenesis defects. We can set the configuration such that the blocked ISV is the only change with the model. Of course, in the actual *kdrl* morphants, we cannot exclude that other significant developmental changes aside from pronounced ISV blockage, such as changes in the heart pressure-velocity relations, or the network elasticity, so we cannot make a well-characterized point-to-point comparison. However, there is a significant increase in the

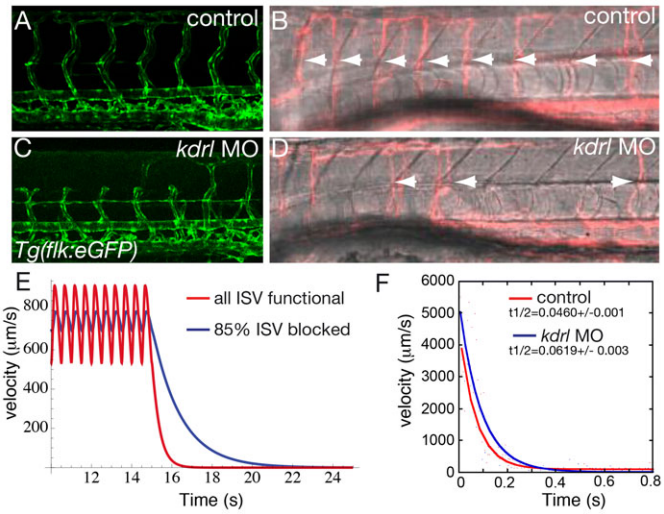

Fig. 4. The viscous resistance of the ISV flow sets the time scale of the flow decay after heart stops. (**A-D**) Visualization of the vascular network shape *Tg(flk1:eGFP)* (A,C) and ISVs with active flow [appearing in pink (false color) after standard deviation projection] (B,D) in controls (A,B) and *kdrl* knock down (C,D) at 3 dpf. White arrowheads indicate active ISVs. (**E**) Plot of the simulated experiment. The heart stops at t=15 seconds for both cases. The axes are flow velocity in µm/second versus time for control (red curve), where all the a/vISV are functional and mutants (blue curve) where 85% of the a/vISV are blocked (zero diameter). (**F**) Example of plots observed for the flow decay after heart stop in one control (red) and one *kdrl* knockdown (blue) embryo.

relaxation time in the *kdrl* morphants, which also suggests this behavior. In other words, the results support the expectation that the ISVs are primarily resistive relative to the DA flow.

Embryonic blood flow propagation relies on blood vessel biomechanics

We next addressed the dynamics of the capacitor effect by characterizing blood cell motion towards the ISV in comparison with the movement of the elastic deformation of the DA. We analyzed the motion of trapped blood cells with the deformation of the DA and found a direct correlation between the orthogonal flow towards the ISV and the endothelial cell wall movement (Fig. 5A-C; supplementary material Movie 7). We plotted the time traces in X and Y for a blood cell close to an ISV (Fig. 5B), and extracted the ϕ from the two signals. As expected, the out-of-phase value for these two traces is Δϕ=38.3°. By comparison with the arterial membrane (Fig. 5C), a strong correlation of motion was seen (Δϕ=9.2°). Thus, relaxation of the DA at the ISV entry is bounded with the additional pressure gradient, indicating that the DA inward motion observed contributes to ISV flow. Altogether, these data show that the slow deflation of the DA lumen creates an additional flow that drives blood cells towards the ISV (Fig. 5D).

Abnormal vascular elasticity is often associated with vascular diseases in adults where compliance is crucial for optimal vascular functions. This opens the possibility that DA distensibility is involved in embryonic vascular function, specifically in helping propagation of flow forces through the network. As a mechanical pump, the heart must do work to move blood through the network. Deformation of the network can thus significantly impact heart effort and could lead to sub-optimal pumping if not well adjusted. To investigate in more detail whether the DA biomechanical properties can affect flow propagation, we used the physical model to test the effect of the DA

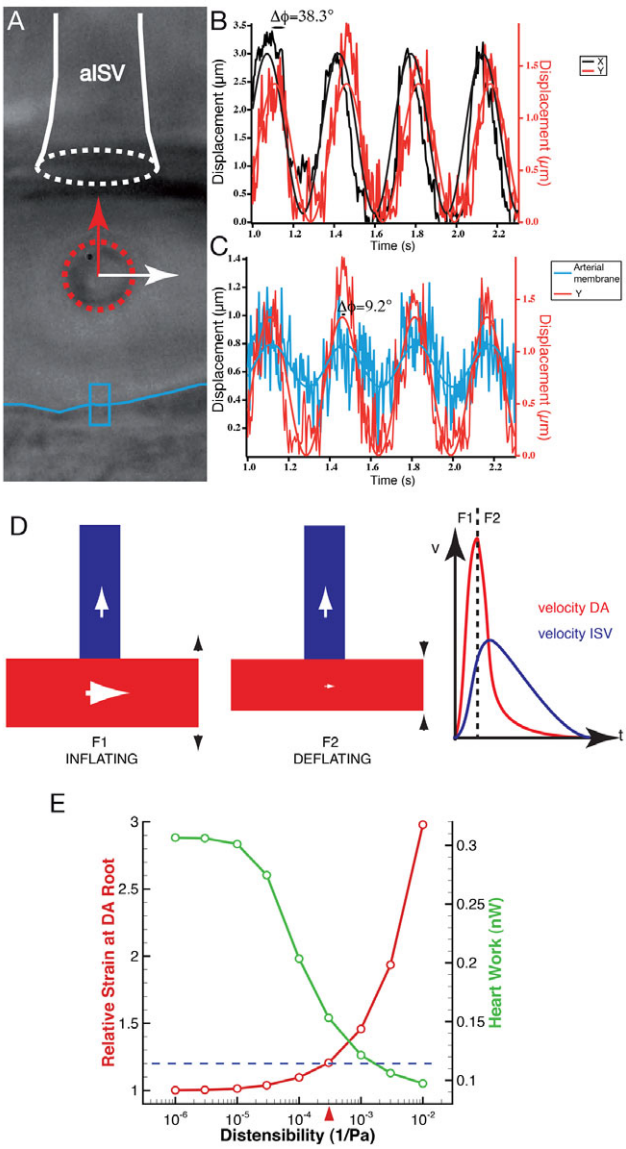

Fig. 5. Dynamic capacitive mechanism in the embryonic vascular network. (**A**) Optical tweezing at the aISV entry in the embryo. The trapped blood cell is outlined by the red dotted circle. The arrows highlight the directions of motion in X (white arrow) and Y (red arrow) of the blood cell. The ISV entry is labeled as a white dotted circle and the blue line labels the ventral DA wall. (**B**) Plot of the oscillations over time in X and Y at the trap point shown in A in the same embryo. (**C**) Plot of the oscillations over time in Y at the trap point shown in A (red line) along with oscillation of the DA cell wall (blue line). The tracked wall corresponds to the blue box in A. The motion towards the ISV is correlated with the DA wall oscillations, showing that the force driving blood cells towards the ISV is coupled with the cyclical deformation of the DA. (**D**) A model for vascular flow at early embryonic stages showing that distensibility of the DA maintains flow in the ISV after heart contraction through its own deflation. The flow direction is labeled with arrows. A first force is needed to inflate the DA (F1) and, as a result of deflation, a second force (F2) is generated that maintains flow steady in the ISV. The observed DA and ISV velocities are plotted according to the force (F1 and F2). (**E**) Heart effort (plotted in green, right y-axis) and strain at the DA root (plotted in red, left y-axis) as a function of the distensibility. Heart effort decreases as elasticity increases. The horizontal blue bar indicates the theoretical strain limit at which vessel will break. The red arrow indicates the measured distensibility, which corresponds to strain of 20%, which is often considered large but not damaging to tissues, suggesting the DA distensibility is optimized near the rupture limit for lowering heart work.

capacitance on heart effort. Using the collected *in vivo* parameters of distensibility, the model predicts that the network elasticity leads to a decrease in the required pumping effort at its best resistivity (Fig. 5E). Thus, the embryonic vascular network is set to decrease heart work through its distensibility, a situation that despite the dominant role of viscosity is functionally similar to the aorta, pulmonary arteries and the larger vessels of the adult vascular network.

DISCUSSION

By exploiting methods for live imaging, quantitative flow analysis and Poiseuille flow modeling, we have identified highly stereotyped flow propagation in the embryonic vascular network. We characterized three major flow properties of the embryonic DA: (1) a change of flow profile from DA to PCV when traversing the ISV network; (2) a mismatched bi-directional flow direction at the ISV entry; (3) blood cell velocities in the ISV do not follow local DA flow at the low velocity peak. Furthermore, we observed: (1) a local endothelial distension of the DA coupled with flow rectification; and (2) an out-of-phase flow for a period after the heart was stopped. Together, these features highlight a capacitive function for the DA, which is unexpected in the absence of inertia at these early embryonic stages. Overall, our analysis provides compelling evidence that DA capacitance leads to two key functions: (1) flow rectification to dampen flow fluctuations in the network; and (2) pressure storage to minimize heart efforts. It is likely that flow rectification through elasticity is a recurring mechanistic strategy to help propagate flow forces in vertebrate organs.

Low Re systems are particularly susceptible to bradycardia and reversing flows, two features that can be observed in the developing cardiovascular system. The simple biomechanical mechanism we describe here allows blood cell motion in the network to be less dependent on the heart maturation state and its unidirectional pumping efficiency. It only necessitates passive deformability of the DA and does not require any muscular control of the blood vessel function. The presented characterization of the early DA elasticity and function provides the foundation for a dynamic role of the embryonic vascular network in propagating flow forces and should help to revisit the mechanics associated with embryonic and adult angiogenesis. Functionally, the observed behavior is analogous to the standard Windkessel model describing the capacitive function of the large elastic arteries in adults at high Reynolds number (Westerhof et al., 2009). We show here this key feature also applies to embryonic arteries, at near zero Reynolds number. Thus, our work provides evidence of biological continuity for a role of vascular elasticity in both the embryonic and adult cardiovascular network, despite the different fluid mechanics operating at these stages. Studying the mechanical and molecular properties of the embryonic vasculature, therefore, may prove relevant to understanding the numerous cardiovascular diseases affecting arterial elasticity, such as atherosclerosis, as well as in the development of new pharmacological strategies targeting these diseases.

Acknowledgements

We thank Emily Steed, Francesco Boselli, Daniel Riveline for thoughtful comments on the manuscript and Stéphane Roth for excellent technical help. We thank C. Wyart, P. Del Bene and S. Schulte-Merker for providing fish stocks. We thank the Institut de Génétique et de Biologie Moléculaire et Cellulaire (IGBMC) imaging center, in particular Pascal Kessler, Marc Koch and Didier Hentsch and Sandrine Geschier and Sylvie Greidler at the IGBMC fish facility.

Funding

This work was supported by the Human Frontier Science Program (HFSP), Institut national de la santé et de la recherche médicale (INSERM), la ligue contre le cancer, Fondation pour la Recherche Médicale (FRM) and the seventh framework program [MC-IRG256549] to J.V., the United States National Science Foundation [CBET 09-32607] to J.B.F. and the Agence National de la Recherche (ANR) [PCVI-2008-0033] to G.C.

Competing interests statement

The authors declare no competing financial interests.

Author contributions

J.V. conceived the project. J.V. and H.A. designed the experiments. H.A. performed the experiments and collected the data. J.B.F. and J.V. together recognized the rectification mechanism. S.H. performed the tweezing experiments with H.A. S.H. analyzed the tweezing experiments. C.R. and H.A. performed the knockdown experiments. D.W., G.C. and C.P. developed the image processing approaches. F.M. provided technical help with the image analysis. S.B. and M.L. developed the realignment programs necessary for the 3D analysis. J.B.F. developed the mathematical model. J.V. and J.B.F. wrote the paper.

Supplementary material

Supplementary material available online at
http://dev.biologists.org/lookup/suppl/doi:10.1242/dev.096768/-/DC1

References

Adamo, L., Naveiras, O., Wenzel, P. L., McKinney-Freeman, S., Mack, P. J., Gracia-Sancho, J., Suchy-Dicey, A., Yoshimoto, M., Lensch, M. W., Yoder, M. C. et al. (2009). Biomechanical forces promote embryonic haematopoiesis. *Nature* **459**, 1131-1135.

Arrenberg, A. B., Stainier, D. Y., Baier, H. and Huisken, J. (2010). Optogenetic control of cardiac function. *Science* **330**, 971-974.

Boon, R. A. and Horrevoets, A. J. (2009). Key transcriptional regulators of the vasoprotective effects of shear stress. *Hamostaseologie* **29**, 39-40, 41-43.

Buschmann, I., Pries, A., Styp-Rekowska, B., Hillmeister, P., Loufrani, L., Henrion, D., Shi, Y., Duelsner, A., Hoefer, I., Gatzke, N. et al. (2010). Pulsatile shear and Gja5 modulate arterial identity and remodeling events during flow-driven arteriogenesis. *Development* **137**, 2187-2196.

Bussmann, J., Bos, F. L., Urasaki, A., Kawakami, K., Duckers, H. J. and Schulte-Merker, S. (2010). Arteries provide essential guidance cues for lymphatic endothelial cells in the zebrafish trunk. *Development* **137**, 2653-2657.

Bussmann, J., Wolfe, S. A. and Siekmann, A. F. (2011). Arterial-venous network formation during brain vascularization involves hemodynamic regulation of chemokine signaling. *Development* **138**, 1717-1726.

Chen, Q., Jiang, L., Li, C., Hu, D., Bu, J. W., Cai, D. and Du, J. L. (2012). Haemodynamics-driven developmental pruning of brain vasculature in zebrafish. *PLoS Biol.* **10**, e1001374.

Corti, P., Young, S., Chen, C. Y., Patrick, M. J., Rochon, E. R., Pekkan, K. and Roman, B. L. (2011). Interaction between alk1 and blood flow in the development of arteriovenous malformations. *Development* **138**, 1573-1582.

Drobczynski, S., Hébraud, P., Munch, J. P. and Harlepp, S. (2009). Design and realization of a high-stability optical tweezer. *Opt. Eng.* **48,** 113601.

Ellertsdóttir, E., Lenard, A., Blum, Y., Krudewig, A., Herwig, L., Affolter, M. and Belting, H. G. (2010). Vascular morphogenesis in the zebrafish embryo. *Dev. Biol.* **341**, 56-65.

Freund, J. B., Goetz, J. G., Hill, K. L. and Vermot, J. (2012). Fluid flows and forces in development: functions, features and biophysical principles. *Development* **139**, 1229-1245.

Galloway, J. L., Wingert, R. A., Thisse, C., Thisse, B. and Zon, L. I. (2005). Loss of gata1 but not gata2 converts erythropoiesis to myelopoiesis in zebrafish embryos. *Dev. Cell* **8**, 109-116.

Habeck, H., Odenthal, J., Walderich, B., Maischein, H., Schulte-Merker, S.; Tübingen 2000 screen consortium (2002). Analysis of a zebrafish VEGF receptor mutant reveals specific disruption of angiogenesis. *Curr. Biol.* **12**, 1405-1412.

Hahn, C. and Schwartz, M. A. (2008). The role of cellular adaptation to mechanical forces in atherosclerosis. *Arterioscler. Thromb. Vasc. Biol.* **28**, 2101-2107.

Hove, J. R., Köster, R. W., Forouhar, A. S., Acevedo-Bolton, G., Fraser, S. E. and Gharib, M. (2003). Intracardiac fluid forces are an essential epigenetic factor for embryonic cardiogenesis. *Nature* **421**, 172-177.

Jin, S. W., Beis, D., Mitchell, T., Chen, J. N. and Stainier, D. Y. (2005). Cellular and molecular analyses of vascular tube and lumen formation in zebrafish. *Development* **132**, 5199-5209.

Jones, E. A. (2011). The initiation of blood flow and flow induced events in early vascular development. *Semin. Cell Dev. Biol.* **22**, 1028-1035.

le Noble, F., Moyon, D., Pardanaud, L., Yuan, L., Djonov, V., Matthijsen, R., Bréant, C., Fleury, V. and Eichmann, A. (2004). Flow regulates arterial-venous differentiation in the chick embryo yolk sac. *Development* **131**, 361-375.

Lin, Y. F., Swinburne, I. and Yelon, D. (2012). Multiple influences of blood flow on cardiomyocyte hypertrophy in the embryonic zebrafish heart. *Dev. Biol.* **362**, 242-253.
Liu, J., Bressan, M., Hassel, D., Huisken, J., Staudt, D., Kikuchi, K., Poss, K. D., Mikawa, T. and Stainier, D. Y. (2010). A dual role for ErbB2 signaling in cardiac trabeculation. *Development* **137**, 3867-3875.
Nicoli, S., Standley, C., Walker, P., Hurlstone, A., Fogarty, K. E. and Lawson, N. D. (2010). MicroRNA-mediated integration of haemodynamics and Vegf signalling during angiogenesis. *Nature* **464**, 1196-1200.
North, T. E., Goessling, W., Peeters, M., Li, P., Ceol, C., Lord, A. M., Weber, G. J., Harris, J., Cutting, C. C., Huang, P. et al. (2009). Hematopoietic stem cell development is dependent on blood flow. *Cell* **137**, 736-748.
Vermot, J., Forouhar, A. S., Liebling, M., Wu, D., Plummer, D., Gharib, M. and Fraser, S. E. (2009). Reversing blood flows act through klf2a to ensure normal valvulogenesis in the developing heart. *PLoS Biol.* **7**, e1000246.
Weinstein, B. M. and Fishman, M. C. (1996). Cardiovascular morphogenesis in zebrafish. *Cardiovasc. Res.* **31**, E17-E24.
Westerhof, N., Lankhaar, J. W. and Westerhof, B. E. (2009). The arterial Windkessel. *Med. Biol. Eng. Comput.* **47**, 131-141.
Yashiro, K., Shiratori, H. and Hamada, H. (2007). Haemodynamics determined by a genetic programme govern asymmetric development of the aortic arch. *Nature* **450**, 285-288.
Zamir, M. (2000). In *The Physics of Pulsatile Flow* (*Biological Physics Series*), pp 147-185. New York, NY: Springer Verlag.